ADVANCED MATERIALS
www.advmat.de

Ultrahigh Rate and Long-Life Sodium-Ion Batteries Enabled by Engineered Surface and Near-Surface Reactions

Changtai Zhao, Chang Yu, Bo Qiu, Si Zhou, Mengdi Zhang, Huawei Huang, Biqiong Wang, Jijun Zhao, Xueliang Sun,* and Jieshan Qiu**

To achieve the high-power sodium-ion batteries, the solid-state ion diffusion in the electrode materials is a highly concerned issue and needs to be solved. In this study, a simple and effective strategy is reported to weaken and degrade this process by engineering the intensified surface and near-surface reactions, which is realized by making use of a sandwich-type nanoarchitecture composed of graphene as electron channels and few-layered MoS_2 with expanded interlayer spacing. The unique 2D sheet-shaped hierarchical structure is capable of shortening the ion diffusion length, while the few-layered MoS_2 with expanded interlayer spacing has more accessible surface area and the decreased ion diffusion resistance, evidenced by the smaller energy barriers revealed by the density functional theory calculations. Benefiting from the shortened ion diffusion distance and enhanced electron transfer capability, a high ratio of surface or near-surface reactions is dominated at a high discharge/charge rate. As such, the composites exhibit the high capacities of 152 and 93 mA h g^{-1} at 30 and 50 A g^{-1}, respectively. Moreover, a high reversible capacity of 684 mA h g^{-1} and an excellent cycling stability up to 4500 cycles can be delivered. The outstanding performance is attributed to the engineered structure with increased contribution of surface or near-surface reactions.

Electrochemical energy storage with both high energy density and high power density is highly demanded for powering the ever-growing fast-charging portable electric devices (PEDs), electric vehicles (EVs) and smart grids.[1] Li-ion batteries (LIBs) have been extensively researched and widely used in the field of PEDs.[2] However, the large-scale applications of LIBs in diverse EVs, and the current and near-future smart grids powered by the renewable energy sources such as solar and wind energy are still restricted by the low power density of the devices, and the limited abundance of lithium resources with uneven distribution.[3] Because of this, sodium-ion batteries (SIBs) have drawn extensive attention as a potential and promising alternative to LIBs for large-scale applications due to the huge advantages of sodium in terms of low cost and large resource availability.[4] However, some big challenges for SIBs need to be addressed, which suffer from more serious problems than LIBs in terms of the achievement of high energy density with high power density. This is because of the large resistance involved in the sluggish kinetics process due to the slow ion transport and electron transfer, particularly, at a high discharge/charge rate that are rooted primarily from larger ionic radius of Na^+.[5] The slow ion transport and electron transfer may not only give rise to a large energy loss, but also lead to huge heat generation which may further result in serious safety problems, which is the case in particular for large devices.[6] As such, it is significant and challenging to enhance the kinetics of SIBs reactions, i.e., to accelerate the mass transport and electron transfer rate in SIBs.[7]

One of the effective strategies to address these bottleneck problems is to tune the reversible reactions occurring on the surface or near-surface of the electrode materials, which can be done by shortening the ion diffusion length and electron transport distance, i.e., to enable the reactions being finished in a short time, which has been proved in electrochemical capacitors with similar electrochemical nature.[8] It is known that the surface reaction contribution is closely related to the morphology and particle size of the electrode materials. Dunn and co-workers have quantitatively evaluated the impact of the anatase TiO_2 particle size on the surface reaction contribution, and confirmed the contribution of surface or near-surface reactions. Such a surface reaction could account for more than 50% of the total reaction when the average particle size is smaller than 10 nm.[9] This leads one to envision that it is possible to

C. Zhao, Prof. C. Yu, B. Qiu, M. Zhang, H. Huang, Prof. J. Qiu
State Key Lab of Fine Chemicals
School of Chemical Engineering
Liaoning Key Lab for Energy Materials and Chemical Engineering
Dalian University of Technology
Dalian 116024, China
E-mail: chang.yu@dlut.edu.cn; jqiu@dlut.edu.cn
C. Zhao, B. Wang, Prof. X. Sun
Department of Mechanical and Materials Engineering
University of Western Ontario
London, ON N6A 5B9, Canada
E-mail: xsun9@uwo.ca
S. Zhou, Prof. J. Zhao
MoE Key Lab of Materials Modification by Laser
Ion and Electron Beams
School of Physics
Dalian University of Technology
Dalian 116024, China

DOI: 10.1002/adma.201702486

further promote the reaction kinetics by synthesizing electrode materials with unique morphology and tuned nanoscale dimensions and increased surface area, which will help to improve the solid-state ion diffusion.[10] To fabricate SIBs with both high power and energy density, anode materials with rational structure are indispensable, in which the contribution of the surface or near surface reactions can be tuned to some extent.

Herein, we report on the design and synthesis of sandwich-type nanoarchitecture in which the MoS_2 is strongly coupled on graphene nanosheets (G@MoS_2-C) via in situ complexation and polymerization reactions guided by graphene that functioned as the structure direction agent, followed by high-temperature gas sulfuration treatment. The strong complexation between Mo ions and polydopamine (PDA) favors the formation of few-layered MoS_2 with expanded interlayer spacing. The carbon species derived from PDA (C-PDA) serves as a binder to strongly couple MoS_2 with the graphene nanosheets. The 2D sheet-shaped structure is capable of shortening the ion diffusion length, while the few-layered MoS_2 with expanded interlayer spacing has more accessible surface area of active materials and the decreased ion diffusion resistance, evidenced by density functional theory (DFT) study, showing that the energy barriers of Na ion diffusion in-between the layers of the MoS_2 with expanded interlayer spacing can be decreased, indicative of the improved reaction kinetics. The graphene intercalated in the hybrid G@MoS_2-C acts as both the channels for fast electron conduction and the substrate for rapid surface reactions. Due to the combined effects mentioned above, the as-made G@MoS_2-C has shown a significant superiority in SIBs with high rate capability, evidenced by the high capacity of 152 and 93 mA h g^{-1} at an ultrahigh current density of 30 and 50 A g^{-1}, respectively. Meanwhile, it also exhibits a high reversible capacity of 684 mA h g^{-1} and excellent cycling stability up to 4500 cycles. The outstanding electrochemical performance of the hybrid G@MoS_2-C is believed to be due to the unique engineered structure with increased contribution of surface or near-surface reactions.

The synthetic strategy of G@MoS_2-C nanosheets involving in situ complexation and polymerization reactions followed by high-temperature gas sulfuration step is shown in **Figure 1**a. Mo ions are firstly coupled with the dopamine via complexation reactions. Then, a fast in situ polymerization reaction of dopamine takes place on the surface of GO nanosheets under alkaline conditions. After that, the gas sulfuration is conducted for the formation of high-crystalline MoS_2.

The representative scanning electron microscopy (SEM) images of the as-made G@MoS_2-C nanosheets (Figure 1b,d) show that the G@MoS_2-C sample has a sheet-shaped structure

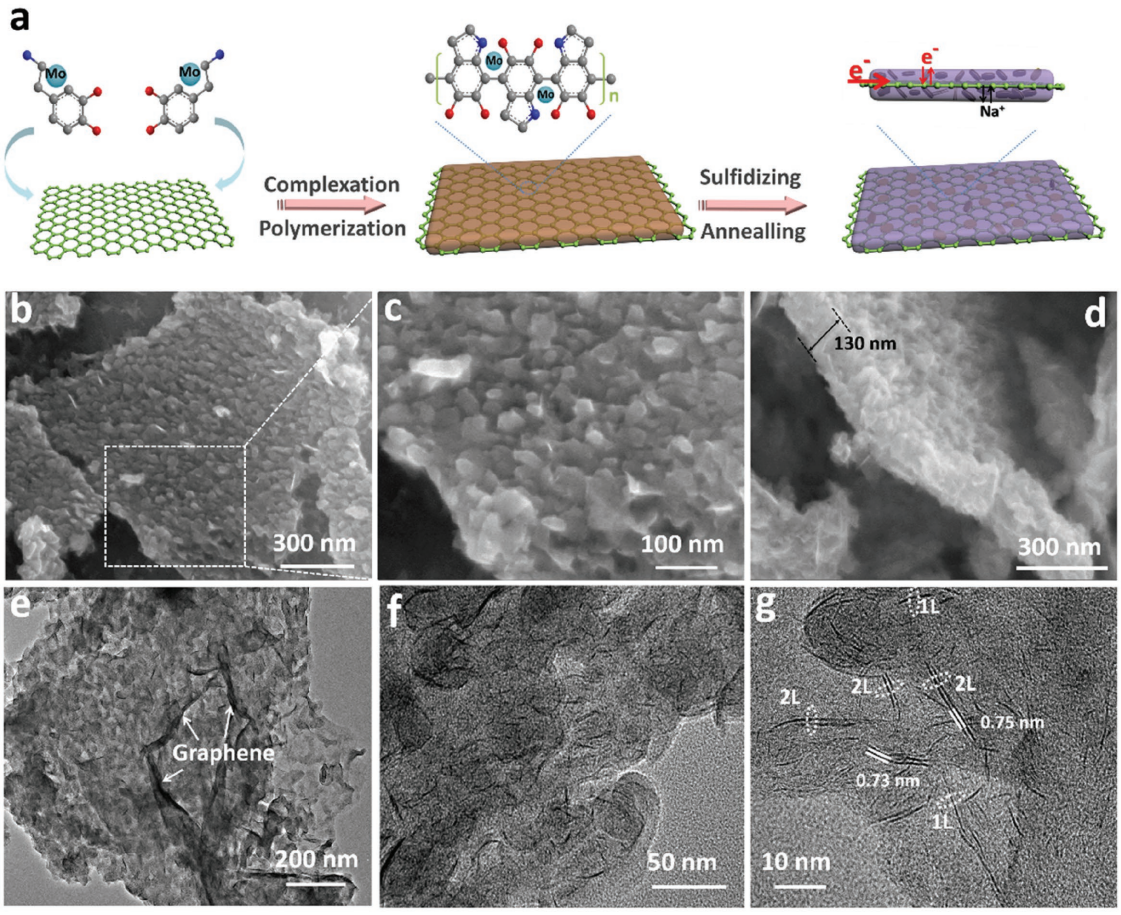

Figure 1. a) Schematic for the formation of G@MoS_2-C nanosheets. b–d) SEM images, e–f) TEM images, and g) HRTEM image of the G@MoS_2-C nanosheets.

with a thickness of ≈130 nm. The magnified SEM image (Figure 1c) shows that the G@MoS_2-C nanosheets are made of many small nanoparticles. For comparison, the pure MoS_2-C composites were also prepared in the absence of graphene template, of which the SEM and transmission electron microscopy (TEM) images are shown in Figure S1 in the Supporting Information. It can be seen that the MoS_2-C composites feature a typical sphere-shaped structure with a diameter of ≈400 nm. Similarly, the MoS_2-C nanospheres are also built of many small nanoparticles. With this information, one may have confidence to believe that the GO nanosheets function as the structure-directed agent, and are responsible for the formation of G@MoS_2-C nanosheets with shortened ion diffusion length for electrodes in SIBs.[11] In the hybrid G@MoS_2-C nanosheets for SIBs, the graphene has another role as the electron conductive channels to ensure rapid electron transfer in the composites.[12] The sheet-shaped structure of the G@MoS_2-C resulted from the graphene-directed growth is further confirmed by the TEM examination, of which the typical images are shown in Figure 1e,f. Specifically, the graphene nanosheets are encapsulated by nanoparticles, yielding a typical sandwich-type structure. The high resolution TEM (HRTEM) image of the G@MoS_2-C nanosheets reveals that these nanoparticles are made of the MoS_2 and C-PDA (Figure 1g). It is assumed here that the C-PDA functions as a bridge or glue to strongly bind MoS_2 onto the surface of the graphene nanosheets. The energy-dispersive X-ray spectrometer elemental mapping also indicates that the MoS_2 is uniformly distributed in the nanosheets (Figure S2, Supporting Information). Interestingly, the MoS_2 in the sandwich-type architecture shows a few-layered feature (≤3 layers), with a lattice spacing of ≈0.73 nm corresponding to the (002) crystal plane of MoS_2 phase, indicative of an expanded interlayer spacing.[13] These features of MoS_2 can be attributed to the strong coordination between Mo ions and PDA, leading to the confined growth of MoS_2 at high temperature, which is also evidenced by the HRTEM image of MoS_2-C nanospheres (Figure S1d, Supporting Information). The porous structure of the as-made G@MoS_2-C nanosheets and MoS_2-C nanospheres was analyzed by nitrogen adsorption technique. As shown in **Figure 2**a, the isotherms for G@MoS_2-C nanosheets are typical type IV, indicative of the balanced pore structure consisting of mesopores and macropores. Moreover, the G@MoS_2-C nanosheets have a Brunauer–Emmett–Teller specific surface area of 126 $m^2\ g^{-1}$, higher than 78 $m^2\ g^{-1}$ of the MoS_2-C nanospheres. The increased surface area is desired for the fast and enhanced adsorption of Na ions in SIBs.

The structure, composition and surface chemical states of the as-made G@MoS_2-C nanosheets were further examined by X-ray diffraction (XRD) technique, Raman spectroscopy, and X-ray photoelectron spectroscopy (XPS). From the XRD patterns of MoS_2-C nanospheres and G@MoS_2-C nanosheets shown in Figure 2b, it is interesting to note that the MoS_2 (002) characteristic peak is missing in both cases, evidencing that the MoS_2 in G@MoS_2-C nanosheets and MoS_2-C nanospheres features

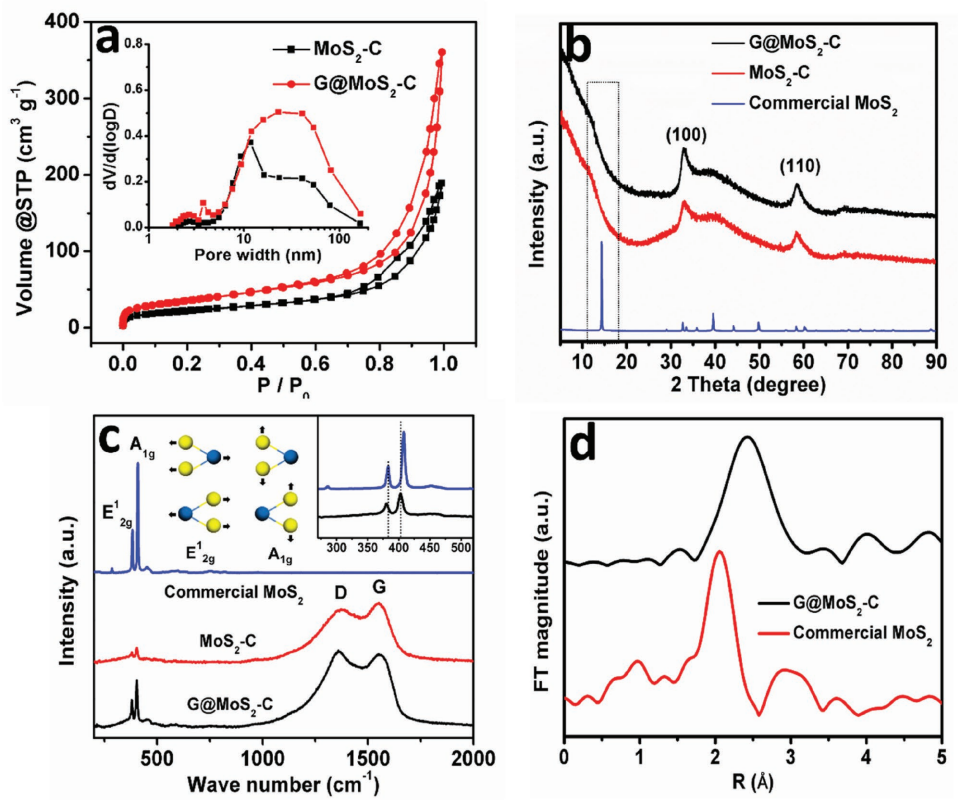

Figure 2. a) Nitrogen adsorption–desorption isotherms and the pore-size distribution (inset) of MoS_2-C nanospheres and G@MoS_2-C nanosheets. b) XRD patterns and c) Raman spectra of the commercial MoS_2, MoS_2-C nanospheres, and G@MoS_2-C nanosheets. d) Mo K-edge Fourier-transformed EXAFS of the commercial MoS_2 and G@MoS_2-C nanosheets.

a few-layered structure, which is also consistent with the TEM results.[14] Moreover, the characteristic peaks of (100) and (110) crystal planes at 32.8° and 58.4° indicate the formation of the hexagonal layered MoS_2.[15] This is further confirmed by the Raman results shown in Figure 2c. The characteristic peaks centering at 380.1 and 403.2 cm^{-1} are assigned to E^1_{2g} and A_{1g} modes of MoS_2 with a typical hexagonal layered structure, respectively.[16] The E^1_{2g} is related to the in-plane vibration of Mo and sulfur atoms, while A_{1g} represents the out-of-plane vibration of sulfur atoms. Compared with the commercial MoS_2, the wave number of A_{1g} characteristic peak has shifted from 408.2 cm^{-1} of commercial MoS_2 to 403.2 cm^{-1} of G@MoS_2-C nanosheets. This obvious shift is mainly attributed to the features of few-layered structure and the expanded interlayer spacing of MoS_2 giving rise to a diminished interlayer van der Waals force which would result in a stronger out-of-plane vibration.[17] The characteristic D-band and G-band peaks indicate the presence of C-PDA and graphene. The extended X-ray absorption fine structure (EXAFS) spectrum of the commercial MoS_2 reveals two apparent characteristic peaks corresponding to the Mo—S and Mo—Mo bond, respectively, which are due to the presence of the nearest neighboring sulfur atoms and Mo atoms around a central Mo atom (Figure 2d). The EXAFS spectrum of the G@MoS_2-C nanosheets shows a well-developed Mo—S peak but relatively weak Mo—Mo peak, which may be due to the few-layered structure and the expanded interlayer spacing of MoS_2 in hybrid G@MoS_2-C.[18] The typical XPS survey spectrum reveals that the G@MoS_2-C nanosheets mainly consist of Mo, S, C, and O elements (Figure S3a, Supporting Information). The two peaks centering at 284.6 and 285.5 eV in the high-resolution C 1s XPS spectra (Figure S3b, Supporting Information) correspond to C—C and C—O bond, respectively. The Mo 3d and S 2p XPS spectra shown in Figure S3c,d in the Supporting Information exhibit typical MoS_2 features. The thermogravimetric analysis (TGA) reveals that the ratio of the MoS_2, C-PDA and graphene in hybrid G@MoS_2-C are 41.8, 53.0, and 5.2%, respectively (Figure S4, Supporting Information). These results mentioned above have demonstrated that the G@MoS_2-C nanosheets with a sandwich-type structure have been successfully synthesized. The unique morphology and the engineered structure and chemical components of G@MoS_2-C nanosheets endow it with outstanding ability for the enhanced contribution of surface or near-surface reactions when employed as the anode materials for SIBs. To be specific, the 2D sheet-shaped structure is capable of shortening the ion diffusion length, and the few-layered MoS_2 with expanded interlayer spacing enables the increase of the accessible surface area of active materials and the decrease of the ion diffusion resistance, which are further confirmed by the DFT calculations. The graphene intercalated in the hybrid G@MoS_2-C acts as the electron conductive channels, which helps to ensure the rapid surface reactions. The strong intimate interaction between MoS_2 and C-PDA helps to effectively prevent the detachment of MoS_2 from the graphene sheets, and facilitate the fast electron transfer during the discharge/charge process.

To explore the potential of the as-made G@MoS_2-C nanosheets as anode materials for SIBs, the electrochemical performance was evaluated by using coin-type cells in a voltage range of 0.01–3.0 V. The cyclic voltammetry (CV) measurements were carried out to analyze the electrochemical reaction mechanism of the G@MoS_2-C nanosheets in SIBs, of which the corresponding curves are shown in Figure S5 in the Supporting Information. In the first cycle, the reduction peaks at 1.05 and 0.82 V correspond to the Na^+ insertion into MoS_2 and the formation of the solid electrolyte interface layer on the surface of the electrode materials.[19] The peak near 0.01 V is assigned to the conversion reaction from MoS_2 to Na_2S and metallic Mo as well as the Na^+ insertion into carbon interlayers. In addition, only one broad oxidation peak is observed at 1.9 V, which is associated with the oxidation of the metallic Mo to MoS_2. The CV curves almost overlap from second to fifth cycle, indicative of the outstanding reversibility of the G@MoS_2-C electrode.

The electrochemical performance of the G@MoS_2-C electrode was further investigated by galvanostatic discharge–charge measurements. **Figure 3**a shows the discharge–charge profiles in the first three cycles at a current density of 100 mA g^{-1}. Surprisingly, a high initial discharge capacity of 1095 mA h g^{-1} is delivered, with a high reversible charge capacity of 684 mA h g^{-1}, indicative of a high material utilization, implying the enough reaction kinetics that is due to the combined effects of the unique structure and the engineered components. The almost overlapped discharge–charge profiles in the second and third cycle indicate an excellent reversibility. The discharge–charge capacity and reversibility of G@MoS_2-C nanosheets were further investigated at a current density of 1 A g^{-1}, of which the results are shown in Figure 3b and Figure S6 in the Supporting Information. The G@MoS_2-C nanosheets have a high reversible capacity of 451 mA h g^{-1} corresponding to a high capacity retention ratio of 76% after 400 cycles. In contrast, the as-made MoS_2-C nanospheres have a low reversible capacity, only 98 mA h g^{-1} after 400 cycles. To further explore the cycling stability of G@MoS_2-C nanosheets, the long-term cycle performance measurement at a large current density of 3 A g^{-1} was performed, of which the results are shown in Figure 3c. Even after 4500 cycles, a high reversible capacity of 253 mA h g^{-1} can be kept, corresponding to a low cyclic fading rate of 0.01% per cycle. The excellent cycling stability is attributed to the unique sheet-shaped structure of G@MoS_2-C composites and the few-layered structure of MoS_2 for accommodating the large volume change and the strongly coupled effects of C-PDA for preventing the detachment of MoS_2 from the graphene substrate. This can be further confirmed by the unchanged structure of the G@MoS_2-C after 100 cycles (Figure S7, Supporting Information).

To figure out the surface and near-surface reaction behaviors of the as-made G@MoS_2-C nanosheets in SIBs, the rate capability of G@MoS_2-C nanosheets was tested at different current densities ranging from 0.1 to 50 A g^{-1}, of which the results are shown in Figure 3d and Figure S8 in the Supporting Information. It is notable that with an increase of the current density, the capacities delivered by the MoS_2-C nanospheres electrode drop sharply. While in the case of the G@MoS_2-C nanosheets, the high capacities of 654, 597, 531, 480, 361, 287, and 201 mA h g^{-1} can be delivered at the current densities of 0.1, 0.2, 0.5, 1, 5, 10, and 20 A g^{-1}, respectively. Even at the ultrahigh current densities of 30 and 50 A g^{-1}, the G@MoS_2-C nanosheets still achieve high reversible capacities of 152 and 93 mA h g^{-1}, respectively, which are much higher than those of the as-made MoS_2-C

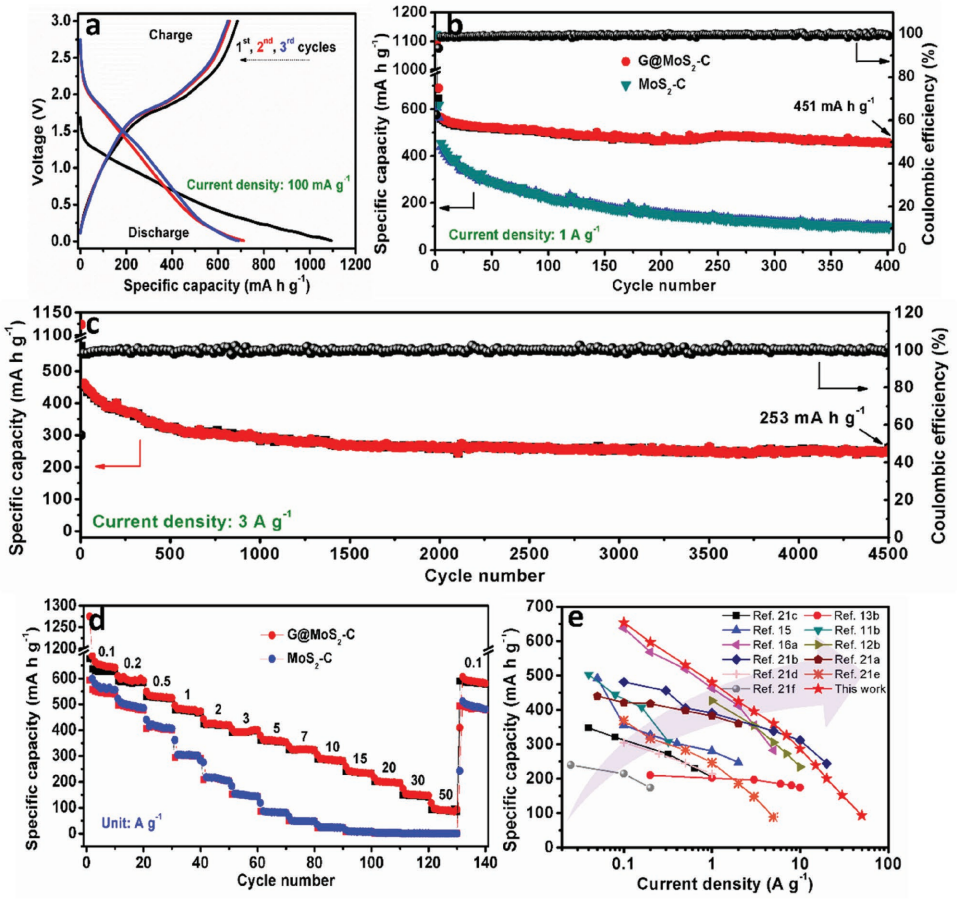

Figure 3. a) Discharge–charge profiles of the G@MoS_2-C electrode for the first three cycles at a current density of 100 mA g^{-1}. b) Cycle performance of the MoS_2-C nanospheres and G@MoS_2-C nanosheets at a current density of 1 A g^{-1}. c) The long-term cycle performance of the G@MoS_2-C nanosheets at a large current density of 3 A g^{-1}. d) Rate performance of the MoS_2-C nanospheres and G@MoS_2-C nanosheets at different densities from 0.1 to 50 A g^{-1}. e) A comparison of the rate performance between this work and the work previously reported in literature.

nanospheres (0.78 and 0.45 mA h g^{-1}) under the same conditions. As shown in **Figure 4**a, the capacity retention rate (the ratio of the discharge capacities at different current densities to the discharge capacity at 0.1 A g^{-1}) of MoS_2-C nanospheres is sensitive to the current density, and quickly drops with an increase of the current density. In sharp contrast, the as-made G@MoS_2-C nanosheets still can keep high capacity retention rates of 23% and 14% even with 300 and 500-fold increase of current density. The high capacity retention rate for the G@MoS_2-C nanosheets would mainly be attributed to surface or near-surface reactions derived from their unique morphology and structure. The possible reaction process involved in electrochemical process is schemed in Figure 4b. With the increase of the discharge/charge rate, the electrochemical reactions more easily occur on the surface of electrode materials instead of bulk phase due to the requirements of fast mass transport and electron transfer. As such, the surface and near-surface reaction behaviors are dominated at a high current density.[4c,20] In the case of G@MoS_2-C, the 2D sheet-shaped structure of composites and the few-layered MoS_2 with expanded interlayer spacing enable the increase of the accessible surface area of active materials and the decrease of the ion diffusion resistance, thus resulting in the high-efficiency utilization of the active materials. The intercalated graphene acts as the electron conductive channels, which is another key factor for the rapid reactions. These features are combined together to make a contribution to the high surface and near-surface reactions even at a large discharge/charge rate, resulting in the high utilization of active materials. However, for the MoS_2-C nanospheres, the story is totally different, evidenced by a low material utilization at a large discharge/charge rate, which is mainly limited by the low surface area and electronic conductivity though the few-layer MoS_2 with expanded interlayer spacing is also present. Figure 3e presents the comparison of the rate capability of the MoS_2-based anode materials in SIBs between this work and previous work in the literature. To the best of our knowledge, the as-made G@MoS_2-C nanosheets exhibit the best rate capability among the MoS_2-based anode materials reported for SIBs thus far.[11b,12b,13b,15,16a,21]

The surface and near-surface reaction behaviors of the G@MoS_2-C nanosheets can be further verified by the electrochemical CV curves and the electrochemical impedance spectroscopy (EIS) measurements. **Figure 5**a shows the CV curves of the G@MoS_2-C nanosheets measured at different scan rates. It can be seen that the CV curves of the G@MoS_2-C nanosheets can keep a similar shape as the scan rate increases, indicative

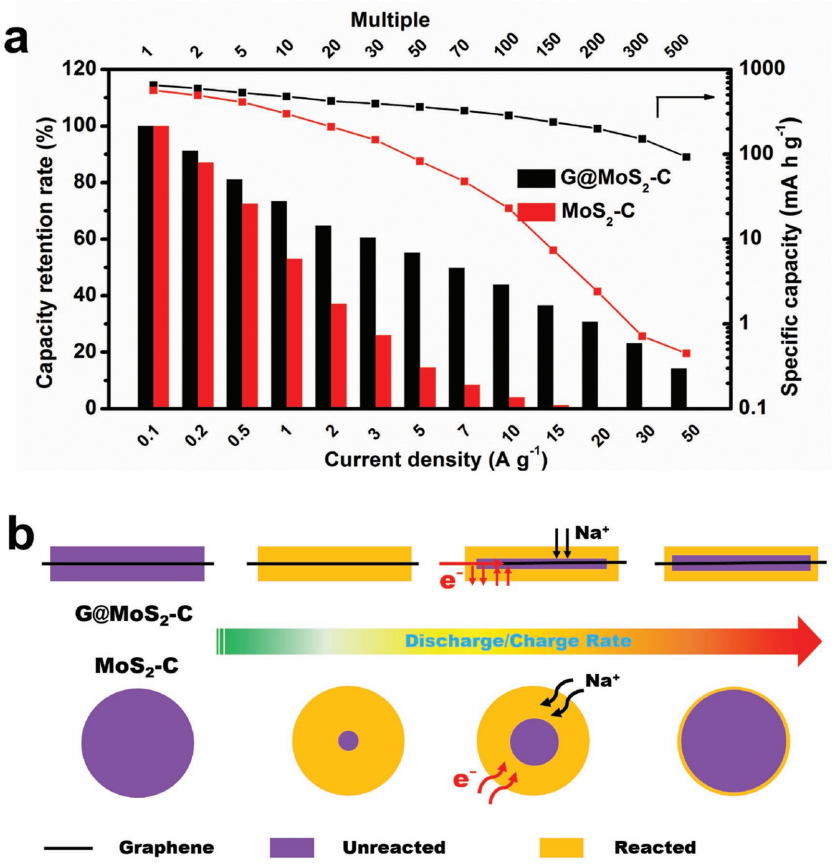

Figure 4. a) The capacity retention rates of the G@MoS_2-C nanosheets and MoS_2-C nanospheres at different current densities. b) Schematic for the electrochemical reactions involved in the hybrid G@MoS_2-C nanosheets and MoS_2-C nanospheres at different discharge/charge rates.

of the excellent adaptability at large scan rates. Compared with that of the G@MoS_2-C nanosheets, the CV curves of MoS_2-C nanospheres at large scan rates show an obvious deformation, indicative of the serious polarizations due to the sluggish reaction kinetics (Figure S9, Supporting Information). Based on the equation of $i = av^b$, the contributions of the surface reactions at different voltages can be evaluated. b is a value ranging from 0.5 to 1, representing the reactions from bulk to the surface or near-surface, respectively.[4c,22] As shown in Figure 5b, at the peak A and peak B (shown in Figure 5a) of the G@MoS_2-C nanosheets, the b value is as high as 0.92 and 0.82, respectively, suggesting the high ratio of the contribution from surface reactions. Moreover, the G@MoS_2-C nanosheets show higher contribution of surface reactions than that of the MoS_2-C nanospheres at a wide voltage range (Figure 5c), which is attributed to the unique sheet-shaped structure and the high conductivity of the G@MoS_2-C nanosheets. The EIS measurements of the as-made G@MoS_2-C nanosheets and MoS_2-C nanospheres were performed at open circuit voltage within a frequency range from 100 kHz to 0.01 Hz. From the Nyquist plots shown in Figure 5d, it can be worked out that the G@MoS_2-C electrode can deliver a smaller diameter of the semicircle in the high-medium frequency region, indicative of smaller charge transfer resistance (R_{ct}) and higher electrical conductivity than that of the MoS_2-C nanospheres electrode.[23] This is attributed to the rapid electron transfer channel effects of graphene in the sandwich-type structure. In the low frequency region of the Nyquist plots, the G@MoS_2-C electrode also presents a larger slope than the MoS_2-C nanospheres, corresponding to a smaller Warburg impedance. This indicates a faster solid-state ion diffusion in the bulk electrode of G@MoS_2-C composites because the unique sheet-shaped structure can decrease the ion diffusion length.[4c,24]

To have a further insight into the positive effects of MoS_2 with expanded interlayer spacing on mitigating diffusion resistance in SIBs, the DFT calculations were conducted by the Vienna ab initio simulation package,[25] and the results are shown in **Figure 6**. To simulate the diffusion process of a Na atom in MoS_2, we considered bulk 2H-MoS_2 in AB stacking with $4 \times 4 \times 1$ unit cells. The Brillouin zone of the supercell was sampled by $3 \times 3 \times 3$ uniform k-point mesh. The climbing-image nudged elastic band (CI-NEB) method was employed to determine the transition state and activation energy for a Na atom to migrate from one position in-between the MoS_2 layers to another (Figure 6a,b). Twelve diffusion sites were used to mimic the diffusion path. The initial (A, diffusion site 0) and final states (E, diffusion site 11) were optimized by only ionic and electronic degrees of freedom using thresholds for the total energy of 10^{-4} eV and force of 0.02 eV $Å^{-1}$. The diffusion barriers at different transition states in-between the layers of the 2H-MoS_2 with different interlayer spacings of 6.17, 6.60, and 7.00 Å are presented in Figure 6c. It can be noted that the highest diffusion energy barrier is delivered in 2H-MoS_2 with the smallest interlayer spacing up to 1.30 eV, which is much higher than that in 2H-MoS_2 with expanded interlayer spacing of 6.60 Å (0.70 eV) and 7.00 Å (0.30 eV), indicating that the expanded interlayer spacing helps to obviously decrease the diffusion resistance. In view of the phase transition from 2H-MoS_2 to 1T-Na_xMoS_2 during Na ions intercalation process,[25] the diffusibility of Na ions in 1T-MoS_2 with different expanded interlayer spacings was also investigated. As shown in Figure S10 in the Supporting Information, the decreased diffusion energy barriers are demonstrated with the increase of the 1T-MoS_2 interlayer spacing. These combined characteristics further demonstrate that the expanded interlayer spacing is in favor of intensifying the mass transportation in SIBs process.

In summary, the sandwich-type G@MoS_2-C nanosheets have been designed and successfully prepared by a novel two-step strategy involving the in situ complexation and polymerization reactions with graphene as the structure-directing agent and the high-temperature gas sulfuration. The 2D sheet-shaped structure helps to shorten the solid-ion diffusion length, the few-layered MoS_2 with expanded interlayer spacing can increase the available and accessible active area, and decrease the ion

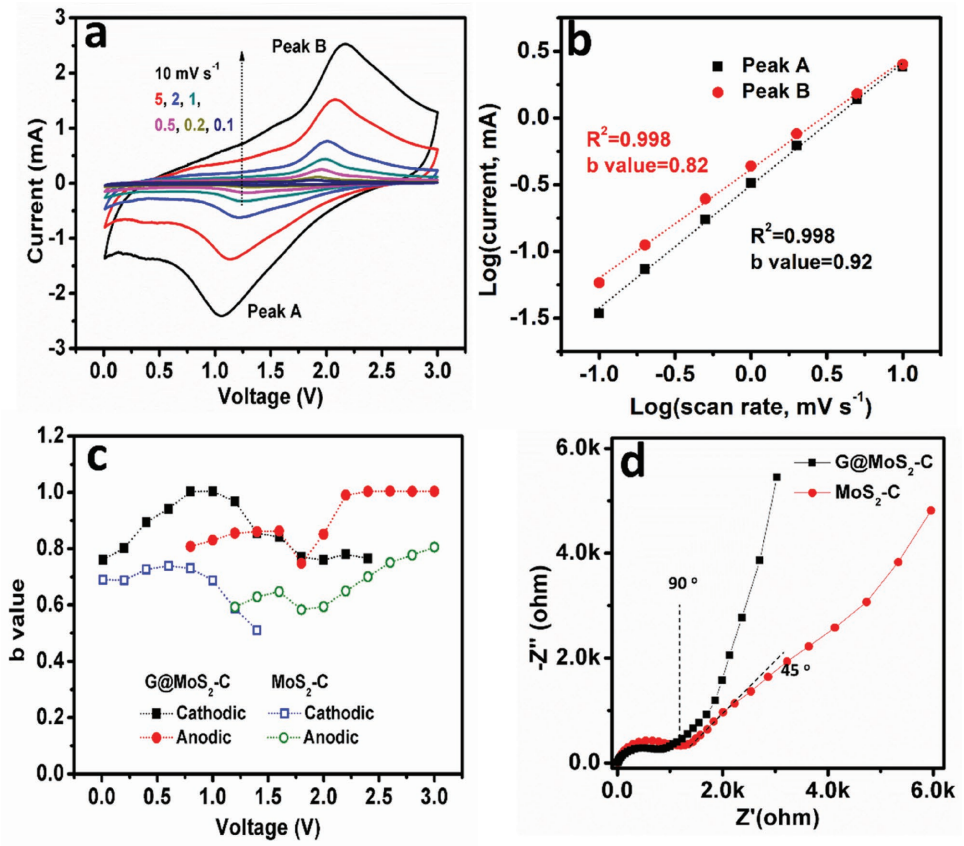

Figure 5. a) CV curves of the G@MoS_2-C nanosheets at different scan rates. b) Current response vs. the scan rate of the G@MoS_2-C nanosheets at the voltages of peak A and peak B. c) *b* value of the MoS_2-C nanospheres and G@MoS_2-C nanosheets at different voltages. d) Nyquist plots of the MoS_2-C nanospheres and G@MoS_2-C nanosheets.

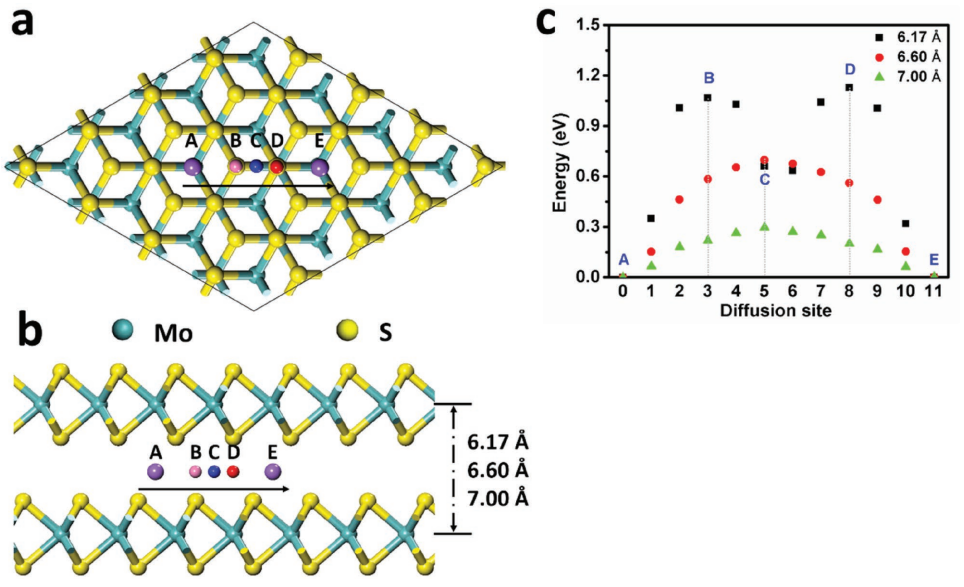

Figure 6. a,b) Schematic illustration for the diffusion process of a Na atom in-between the MoS_2 layers with different interlayer spacings of 6.17, 6.60, and 7.00 Å, respectively. c) The curves of diffusion energy barriers at different transition states: the MoS_2 with different interlayer spacing of 6.17 (black), 6.60 (red), and 7.00 Å (green).

diffusion resistance, evidenced by the smaller energy barriers revealed by the DFT calculations. The graphene in the sandwich-type structure as the electron channels helps to enhance electrical conductivity of the whole composites. Benefiting from these structure merits, the G@MoS_2-C nanosheets show ultrahigh surface or near-surface reaction contributions, evidenced by the high rate capacity of 93 mA h g^{-1} at 50 A g^{-1}. The present work has demonstrated a novel strategy to configure the MoS_2 composites with unique structure, and may open a new way for design of high-rate anode materials for SIBs.

Supporting Information

Supporting Information is available from the Wiley Online Library or from the author.

Acknowledgements

This work was partly supported by the NSFC (Nos. 21522601, U1508201, 21361162004), Natural Sciences and Engineering Research Council of Canada (NSERC), Canada Research Chair Program (CRC), Canada Foundation for Innovation (CFI), Ontario Research Fund (ORF), and the University of Western Ontario. C. Zhao was supported by the Chinese Scholarship Council.

Conflict of Interest

The authors declare no conflict of interest.

Keywords

graphene, high rate capability, MoS_2, sodium ion batteries, surface reactions

Received: May 4, 2017
Revised: October 22, 2017
Published online: January 8, 2018

[1] a) C. Yang, X. Ou, X. Xiong, F. Zheng, R. Hu, Y. Chen, M. Liu, K. Huang, *Energy Environ. Sci.* **2017**, *10*, 107; b) S. Yuan, Y.-H. Zhu, W. Li, S. Wang, D. Xu, L. Li, Y. Zhang, X.-B. Zhang, *Adv. Mater.* **2017**, *29*, 1602469; c) C. Zhao, C. Yu, S. Liu, J. Yang, X. Fan, H. Huang, J. Qiu, *Adv. Funct. Mater.* **2015**, *25*, 6913; d) C. Zhao, Y. Lu, Y. Li, L. Jiang, X. Rong, Y. Hu, H. Li, L. Chen, *Small Methods* **2017**, *1*, 1600063.

[2] a) Y. Liu, H. Wang, L. Cheng, N. Han, F. Zhao, P. Li, C. Jin, Y. Li, *Nano Energy* **2016**, *20*, 168; b) Y. Wang, D. Kong, W. Shi, B. Liu, G. J. Sim, Q. Ge, H. Y. Yang, *Adv. Energy Mater.* **2016**, *6*, 1601057; c) S. Wang, L. Xia, L. Yu, L. Zhang, H. Wang, X. W. Lou, *Adv. Energy Mater.* **2016**, *6*, 1502217; d) Y. Li, Y.-S. Hu, M.-M. Titirici, L. Chen, X. Huang, *Adv. Energy Mater.* **2016**, *6*, 1600659.

[3] a) Z. Liu, X.-Y. Yu, X. W. Lou, U. Paik, *Energy Environ. Sci.* **2016**, *9*, 2314; b) N. Yabuuchi, K. Kubota, M. Dahbi, S. Komaba, *Chem. Rev.* **2014**, *114*, 11636; c) Y. Zheng, T. Zhou, C. Zhang, J. Mao, H. Liu, Z. Guo, *Angew. Chem., Int. Ed.* **2016**, *55*, 3408; d) H. Hou, L. Shao, Y. Zhang, G. Zou, J. Chen, X. Ji, *Adv. Sci.* **2017**, *4*, 1600243.

[4] a) H.-Y. Chen, N. Bucher, S. Hartung, L. Li, J. Friedl, H.-P. Liou, C.-L. Sun, U. Stimming, M. Srinivasan, *Adv. Mater. Interfaces* **2016**, *3*, 1600357; b) W. Luo, F. Shen, C. Bommier, H. Zhu, X. Ji, L. Hu, *Acc. Chem. Res.* **2016**, *49*, 231; c) C. Zhao, C. Yu, M. Zhang, H. Huang, S. Li, X. Han, Z. Liu, J. Yang, W. Xiao, J. Liang, X. Sun, J. Qiu, *Adv. Energy Mater.* **2017**, *7*, 1602880.

[5] a) J. Sun, H.-W. Lee, M. Pasta, H. Yuan, G. Zheng, Y. Sun, Y. Li, Y. Cui, *Nat. Nanotechnol.* **2015**, *10*, 980; b) J. Yang, X. Zhou, D. Wu, X. Zhao, Z. Zhou, *Adv. Mater.* **2017**, *29*, 1604108; c) K. Zhang, M. Park, L. Zhou, G.-H. Lee, W. Li, Y.-M. Kang, J. Chen, *Adv. Funct. Mater.* **2016**, *26*, 6728.

[6] P. V. Braun, J. Cho, J. H. Pikul, W. P. King, H. Zhang, *Curr. Opin. Solid State Mater. Sci.* **2012**, *16*, 186.

[7] a) D. Xie, X. Xia, Y. Zhong, Y. Wang, D. Wang, X. Wang, J. Tu, *Adv. Energy Mater.* **2016**, *6*, 1601804; b) C. Zhao, C. Yu, M. Zhang, Q. Sun, S. Li, M. Banis, X. Han, Q. Dong, J. Yang, G. Wang, X. Sun, J. Qiu, *Nano Energy* **2017**, *41*, 66.

[8] a) D. Chao, C. Zhu, P. Yang, X. Xia, J. Liu, J. Wang, X. Fan, S. V. Savilov, J. Lin, H. J. Fan, Z. X. Shen, *Nat. Commun.* **2016**, *7*, 12122; b) T. Brezesinski, J. Wang, J. Polleux, B. Dunn, S. H. Tolbert, *J. Am. Chem. Soc.* **2009**, *131*, 1802.

[9] J. Wang, J. Polleux, J. Lim, B. Dunn, *J. Phys. Chem. C* **2007**, *111*, 14925.

[10] a) C. Chen, Y. Wen, X. Hu, X. Ji, M. Yan, L. Mai, P. Hu, B. Shan, Y. Huang, *Nat. Commun.* **2015**, *6*, 6929; b) X. Song, X. Li, Z. Bai, B. Yan, D. Li, X. Sun, *Nano Energy* **2016**, *26*, 533; c) J. B. Cook, H.-S. Kim, Y. Yan, J. S. Ko, S. Robbennolt, B. Dunn, S. H. Tolbert, *Adv. Energy Mater.* **2016**, *6*, 1501937.

[11] a) Y. Zhang, P. Zhu, L. Huang, J. Xie, S. Zhang, G. Cao, X. Zhao, *Adv. Funct. Mater.* **2015**, *25*, 481; b) D. Su, S. Dou, G. Wang, *Adv. Energy Mater.* **2015**, *5*, 1401205.

[12] a) C. Zhang, X. Wang, Q. Liang, X. Liu, Q. Weng, J. Liu, Y. Yang, Z. Dai, K. Ding, Y. Bando, J. Tang, D. Golberg, *Nano Lett.* **2016**, *16*, 2054; b) S. H. Choi, Y. N. Ko, J.-K. Lee, Y. C. Kang, *Adv. Funct. Mater.* **2015**, *25*, 1780; c) F. Zhang, C. Xia, J. Zhu, B. Ahmed, H. Liang, D. B. Velusamy, U. Schwingenschlögl, H. N. Alshareef, *Adv. Energy Mater.* **2016**, *6*, 1601188.

[13] a) T. S. Sahu, S. Mitra, *Sci. Rep.* **2015**, *5*, 12571; b) Z. Hu, L. Wang, K. Zhang, J. Wang, F. Cheng, Z. Tao, J. Chen, *Angew. Chem., Int. Ed.* **2014**, *53*, 12794.

[14] a) C. Zhu, X. Mu, P. A. van Aken, Y. Yu, J. Maier, *Angew. Chem., Int. Ed.* **2014**, *53*, 2152; b) J. Wang, J. Liu, D. Chao, J. Yan, J. Lin, Z. X. Shen, *Adv. Mater.* **2014**, *26*, 7162.

[15] Y.-X. Wang, S.-L. Chou, D. Wexler, H.-K. Liu, S.-X. Dou, *Chem. Eur. J.* **2014**, *20*, 9607.

[16] a) J. Wang, J. Liu, H. Yang, D. Chao, J. Yan, S. V. Savilov, J. Lin, Z. X. Shen, *Nano Energy* **2016**, *20*, 1; b) Y.-L. Ding, P. Kopold, K. Hahn, P. A. van Aken, J. Maier, Y. Yu, *Adv. Mater.* **2016**, *28*, 7774; c) C. Yu, X. Meng, X. Song, S. Liang, Q. Dong, G. Wang, C. Hao, X. Yang, T. Ma, P. M. Ajayan, J. Qiu, *Carbon* **2016**, *100*, 474.

[17] S. Zhang, B. V. R. Chowdari, Z. Wen, J. Jin, J. Yang, *ACS Nano* **2015**, *9*, 12464.

[18] D. H. Youn, J.-W. Jang, J. Y. Kim, J. S. Jang, S. H. Choi, J. S. Lee, *Sci. Rep.* **2014**, *4*, 5492.

[19] J. Wang, C. Luo, T. Gao, A. Langrock, A. C. Mignerey, C. Wang, *Small* **2015**, *11*, 473.

[20] a) V. Augustyn, P. Simon, B. Dunn, *Energy Environ. Sci.* **2014**, *7*, 1597; b) C. Chen, H. Xu, T. Zhou, Z. Guo, L. Chen, M. Yan, L. Mai, P. Hu, S. Cheng, Y. Huang, J. Xie, *Adv. Energy Mater.* **2016**, *6*, 1600322.

[21] a) Z.-T. Shi, W. Kang, J. Xu, L.-L. Sun, C. Wu, L. Wang, Y.-Q. Yu, D. Y. W. Yu, W. Zhang, C.-S. Lee, *Small* **2015**, *11*, 5667; b) Y. Lu, Q. Zhao, N. Zhang, K. Lei, F. Li, J. Chen, *Adv. Funct. Mater.* **2016**, *26*, 911; c) X. Xie, T. Makaryan, M. Zhao, K. L. Van Aken, Y. Gogotsi, G. Wang, *Adv. Energy Mater.* **2016**, *6*, 1502161; d) W. Qin, T. Chen,

L. Pan, L. Niu, B. Hu, D. Li, J. Li, Z. Sun, *Electrochim. Acta* **2015**, *153*, 55; e) X. Xiong, W. Luo, X. Hu, C. Chen, L. Qie, D. Hou, Y. Huang, *Sci. Rep.* **2015**, *5*, 9254; f) L. David, R. Bhandavat, G. Singh, *ACS Nano* **2014**, *8*, 1759.

[22] a) T. Brezesinski, J. Wang, S. H. Tolbert, B. Dunn, *Nat. Mater.* **2010**, *9*, 146; b) P. Yu, C. Li, X. Guo, *J. Phys. Chem. C* **2014**, *118*, 10616; c) K. Zhang, M. Park, L. Zhou, G.-H. Lee, J. Shin, Z. Hu, S.-L. Chou, J. Chen, Y.-M. Kang, *Angew. Chem., Int. Ed.* **2016**, *55*, 12822.

[23] a) H. Hou, C. E. Banks, M. Jing, Y. Zhang, X. Ji, *Adv. Mater.* **2015**, *27*, 7861; b) X. Wang, L. Fan, D. Gong, J. Zhu, Q. Zhang, B. Lu, *Adv. Funct. Mater.* **2016**, *26*, 1104.

[24] a) C. Wu, Y. Jiang, P. Kopold, P. A. van Aken, J. Maier, Y. Yu, *Adv. Mater.* **2016**, *28*, 7276; b) L. Wang, X. Bi, S. Yang, *Adv. Mater.* **2016**, *28*, 7672.

[25] M. Mortazavi, C. Wang, J. Deng, V. B. Shenoy, N. V. Medhekar, *J. Power Sources* **2014**, *268*, 279.